Improvement of High-Resolution Satellite Rainfall Product for Typhoon Morakot (2009) over Taiwan

AINA TANIGUCHI, SHOICHI SHIGE, MUNEHISA K. YAMAMOTO, AND TOMOAKI MEGA

Graduate School of Science, Kyoto University, Kyoto, Japan

SATOSHI KIDA, TAKUJI KUBOTA, AND MISAKO KACHI

Earth Observation Research Center, Japan Aerospace Exploration Agency, Tsukuba, Japan

TOMOO USHIO

Department of Electrical, Electronic, and Information Engineering, Osaka University, Suita, Japan

KAZUMASA AONASHI

Meteorological Research Institute, Japan Meteorological Agency, Tsukuba, Japan

(Manuscript received 13 March 2013, in final form 27 July 2013)

ABSTRACT

The authors improve the high-resolution Global Satellite Mapping of Precipitation (GSMaP) product for Typhoon Morakot (2009) over Taiwan by using an orographic/nonorographic rainfall classification scheme. For the estimation of the orographically forced upward motion used in the orographic/nonorographic rainfall classification scheme, the optimal horizontal length scale for averaging the elevation data is examined and found to be about 50 km. It is inferred that as the air ascends en masse on the horizontal scale, it becomes unstable and convection develops. The orographic/nonorographic rainfall classification scheme is extended to the GSMaP algorithm for all passive microwave radiometers in orbit, including not just microwave imagers but also microwave sounders. The retrieved rainfall rates, together with infrared images, are used for the high-resolution rainfall products, which leads to much better agreement with rain gauge observations.

1. Introduction

Typhoon Morakot (2009) produced a huge amount of rainfall and had a catastrophic impact on Taiwan (Wu and Yang 2011; Wu 2013). The extreme amount of rainfall triggered severe flooding and enormous mudslides in southern Taiwan, which caused so-called gauge denial situations, where ground rain gauges were either washed away or damaged.

Under gauge denial situations, one possible substitute for conventional gauges for surface hydrological applications, such as flood and landslides, is high-resolution satellite rainfall products (0.1°–0.25° latitude–longitude and 0.5–3 hourly), available by combining data obtained by microwave radiometers (MWRs) in low Earth orbit and by infrared radiometers (IRs). Following the great success of the Tropical Rainfall Measuring Mission (TRMM; Kummerow et al. 1998), which carries the first spaceborne precipitation radar (PR; Kozu et al. 2001; Okamoto 2003), the development of high-resolution satellite rainfall products has accelerated (see reviews in Gebremichael and Hossain 2010). However, Chen et al. (2013) suggested that high-resolution satellite rainfall products, such as the TRMM Multisatellite Precipitation Analysis (TMPA; Huffman et al. 2007), the Climate Prediction Center Morphing product (CMORPH; Joyce et al. 2004), and the Precipitation Estimation from Remotely Sensed Information using Artificial Neural Networks (Sorooshian et al. 2000), cannot be used as a substitute because these products demonstrated poor performance over the mountainous terrain of Taiwan during heavy rainfall events.

Ge et al. (2010) simulated this event numerically and concluded that the extreme amount and distribution of

Corresponding author address: Shoichi Shige, Graduate School of Science, Kyoto University, Kiashirakawa-Oiwake, Sakyo, Kyoto 606-8502, Japan.
E-mail: shige@kugi.kyoto-u.ac.jp

DOI: 10.1175/JHM-D-13-047.1

rainfall was mainly a response to Taiwan's terrain and a strong monsoon surge. The identification of the poor performance of high-resolution satellite rainfall products over mountainous areas can be found in Kubota et al. (2009) for Japan and in Dinku et al. (2010) for Africa and South America. Kubota et al. (2009) suggested that one of the main reasons for such errors is that MWR algorithms might underestimate heavy rainfall associated with shallow orographic rainfall systems.

There have been few studies on the improvement of MWR rain retrieval for mountainous regions. Following the study by Vicente et al. (2002) on the improvement of IR-based rain retrieval, Kwon et al. (2008) developed topographic correction factors, as a function of terrain slope, low-level wind, and moisture parameters for the terrain of the Korean Peninsula in the Goddard profiling (GPROF) algorithm (Kummerow et al. 2001; McCollum and Ferraro 2003; Olson et al. 2006; Wang et al. 2009), which is the TRMM Microwave Imager (TMI) facility algorithm. Recently, Shige et al. (2013, hereafter S13) improved the performance of rainfall estimates made by the Global Satellite Mapping of Precipitation (GSMaP) MWR algorithm (hereafter GSMaP_MWR; Aonashi et al. 2009; Kubota et al. 2007) from TMI data for the Kii Peninsula, which is a region of heavy precipitation in Japan for which satellite methods of estimating the maximum rainfall amounts have been shown to be poor (Negri and Adler 1993; Kubota et al. 2009). They did not introduce orographic correction factors to the GSMaP_MWR algorithm, but rather they incorporated a dynamic selection of lookup tables (LUTs) that are appropriate for heavy orographic rainfall based on an orographic/nonorographic rainfall classification scheme.

In this study, the GSMaP_MWR algorithm with the orographic/nonorographic rainfall classification scheme, developed by S13, is applied to Typhoon Morakot (2009). As a first step, we focus on observations derived from the TRMM satellite overpass of Typhoon Morakot over Taiwan. Second, the GSMaP_MWR algorithm is applied to MWRs on other satellites, and then high temporal resolution interpolation for the GSMaP_MWR products is obtained from cloud-top motion derived from two successive IR images and a Kalman filter (hereafter referred to as GSMaP_MVK; Ushio et al. 2009). The GSMaP_MVK estimates are compared with a relatively dense rain gauge network over Taiwan Island.

2. Data

The GSMaP_MWR algorithm consists of a forward calculation part to calculate LUTs showing the relationship between the rainfall rate and brightness temperatures Tb with a radiative transfer model (RTM) and a retrieval part to estimate the precipitation rate from the observed Tb using the LUTs. Here, the GSMaP_MWR overland algorithm is described. For further details, refer to Aonashi et al. (2009).

From forward calculations with a four-stream RTM (Liu 1998), LUTs showing the relationship between the rainfall rate and Tb were computed daily for $5.0° \times 5.0°$ latitude–longitude boxes. The RTM calculation requires information on atmospheric variables and precipitation-related variables. In this study, atmospheric temperature, freezing-level height (FLH), and surface temperature are adapted from the Japan Meteorological Agency (JMA) Climate Data Assimilation System (JCDAS), which is the continuation of the Japanese 25-yr Reanalysis project (JRA-25; Onogi et al. 2007).

The convective and stratiform precipitation models for precipitation-related variables such as hydrometeor profiles are constructed for seven land precipitation types. Precipitation types are determined in terms of the stratiform pixel ratio, stratiform rain ratio, precipitation area, precipitation-top height, rain intensity, and diurnal cycle, obtained from the PR data, together with the ratio of PR precipitation rates and TRMM Lightning Imaging Sensor flash rates (Takayabu 2006, 2008). Global distributions of the precipitation types in $2.5° \times 2.5°$ latitude–longitude boxes are classified statistically trimonthly. The convective and stratiform precipitation profiles of PR data are averaged over prescribed precipitation ranges for each precipitation type. In this averaging, profiles relative to the FLH are used to exclude the effects of atmospheric temperature variations. The database of precipitation types and profiles makes it possible for the algorithm to accommodate trimonthly variations in typical hydrometeor profiles.

First, we focus on observations derived from a TRMM satellite overpass of Typhoon Morakot over Taiwan. A comparison of TMI estimates with nearly coincident PR estimates is very useful for the development and validation of rainfall retrievals for TMI. For the comparison with the GSMaP_MWR estimates, we use the PR 2A25 version 6 product (Iguchi et al. 2009) and the TMI 2A12 version 6 product derived from the GPROF algorithm (Kummerow et al. 2001; McCollum and Ferraro 2003; Olson et al. 2006; Wang et al. 2009).

Observations derived from other microwave imagers, such as the Advanced Microwave Scanning Radiometer for the Earth Observing System (AMSR-E), the Special Sensor Microwave Imager (SSM/I), and Special Sensor Microwave Imager/Sounder (SSMIS) as well as the Advanced Microwave Sounding Unit (AMSU) microwave sounder, are used to obtain high-resolution rainfall maps of Typhoon Morakot over Taiwan. The GSMaP_MWR over land algorithm for AMSU (Shige et al. 2009) is

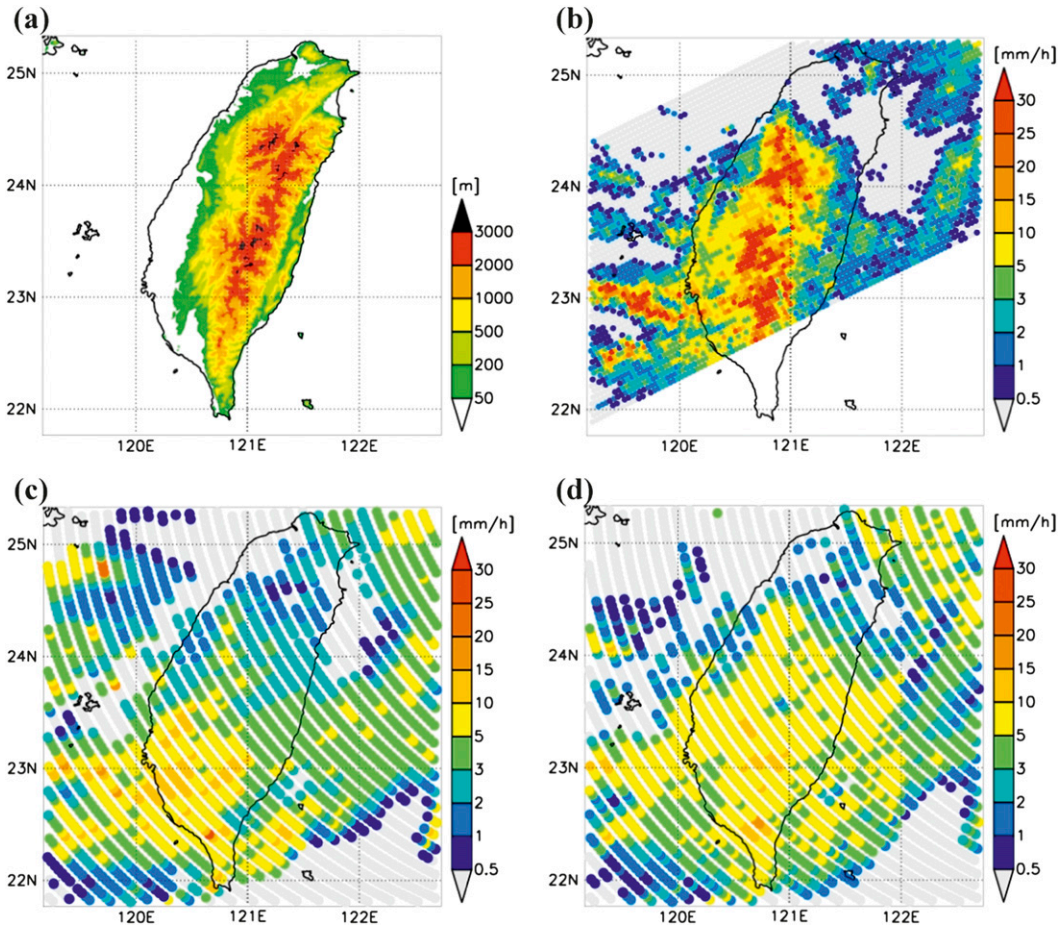

FIG. 1. Observations derived from a TRMM satellite overpass of Typhoon Morakot over Taiwan area on 8 August 2009 (TRMM orbit 66832). (a) SRTM30 elevation (m), (b) PR 2A25 near-surface rain (mm h^{-1}), (c) GPROF surface rain (mm h^{-1}), and (d) GSMaP_MWR surface rain (mm h^{-1}) estimated from TMI-observed Tbs. The observation times of PR and TMI were 2043 and 2044 UTC, respectively.

almost the same as that for microwave imagers, except for the process of making the LUTs, where differences in scanning geometry between imagers (conical scanning) and sounders (cross-track scanning) are taken into account.

High temporal resolution interpolation for the GSMaP_MWR products (GSMaP_MVK) is obtained with cloud-top motion derived from two successive IR images and a Kalman filter (Ushio et al. 2009). For the comparison with the GSMaP_MVK estimates, we use the TMPA near-real-time version product (3B42RT). Multisatellite MWR rainfall estimates are calibrated by the TRMM estimates, and the geostationary IR rainfall estimates are made by calibrating IR Tbs with the MWR rainfall estimates using a histogram-matching technique (Huffman et al. 2007). The TMPA 3B42RT rain estimates consist of the MWR estimates where available and the IR estimates otherwise. The rain gauge data are not used in the TMPA 3B42RT products for calibration. The temporal resolution is 3 hours, and the spatial resolution is 0.25° × 0.25° latitude–longitude. We also use hourly precipitation data observed at 403 rain gauge stations in Taiwan, which are provided by Taiwan's Central Weather Bureau. The geographical distribution of the rain gauge stations is mentioned later.

3. Results and discussion

a. TRMM overpass

Figure 1 shows the observations derived from a TRMM satellite overpass of Typhoon Morakot over Taiwan on 8 August 2009. High surface rainfall rates of >25 mm h^{-1} were detected on the western side of the Central Mountain Range running southwest to northeast in Taiwan (Fig. 1a) in the PR data (Fig. 1b). Large surface rainfall

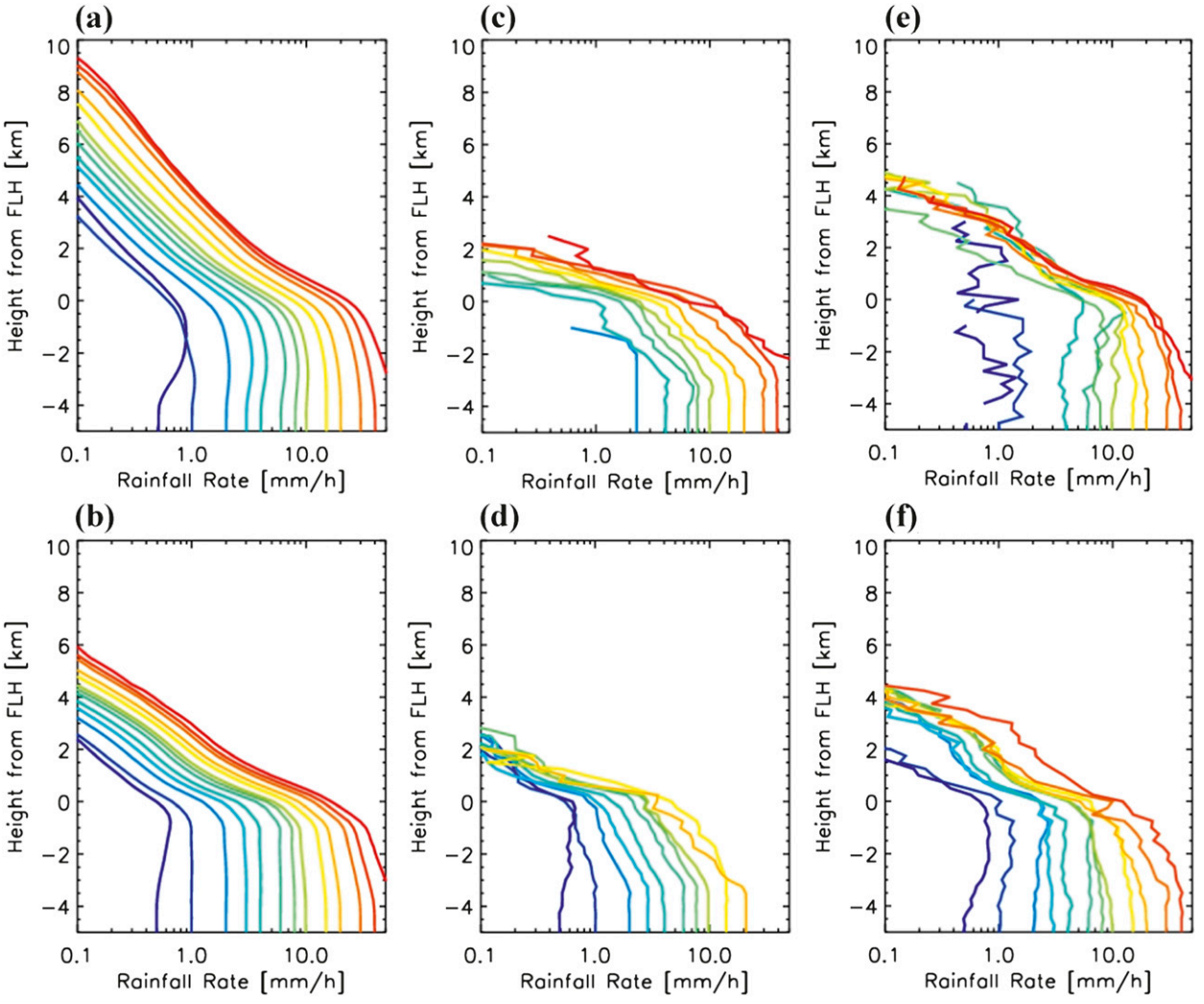

FIG. 2. Precipitation profiles for (a) convective and (b) stratiform rain used by the original GSMaP_MWR algorithm to produce a LUT for rain retrieval in the case shown in Fig. 1d, (c) convective and (d) stratiform rain for the orographic rainfall case in the Kii Peninsula derived by S13, and (e) convective and (f) stratiform rain over the land of Taiwan observed by the PR for the case shown in Fig. 1b. The abscissa is the rainfall rate (mm h^{-1}) and the ordinate is the height difference (km) from the FLH. Each curve is colored relative to surface rainfall rate.

events, such as those seen in the PR data, were not detected in the surface rainfall data retrieved from the TMI data by the GPROF algorithm (Fig. 1c), nor in the original GSMaP_MWR algorithm surface rainfall estimated from the TMI-observed Tbs (Fig. 1d).

In the GSMaP_MWR algorithm, the surface rainfall estimate is obtained mainly through estimates from the polarization-corrected temperatures (Spencer et al. 1989) at 85 GHz (PCT85) using LUTs, which depend greatly on precipitation profiles inputted into the RTM calculations. S13 compared the precipitation profiles used in the original GSMaP_MWR (Figs. 2a,b) with the orographic precipitation profiles (Figs. 2c,d) observed by PR over the Kii Peninsula and used for the improvement of orographic rainfall estimates. The orographic precipitation profiles had much lower precipitation top heights than those of the original profiles, which was consistent with the fact that heavy rainfall from shallow clouds in this area has been reported by previous studies (Takeda et al. 1976; Takeda and Takase 1980; Sakakibara 1981). Warm-rain processes are enhanced by low-level orographic lifting of maritime air, such that rainfall develops at a low level in the growing convective elements and precipitates while the clouds are still developing. PCT85 in the LUT calculated from the original precipitation profiles decreases more rapidly with rainfall rate than that in the LUT calculated from orographic precipitation profiles (see Fig. 3 of S13) because the thickness of the ice

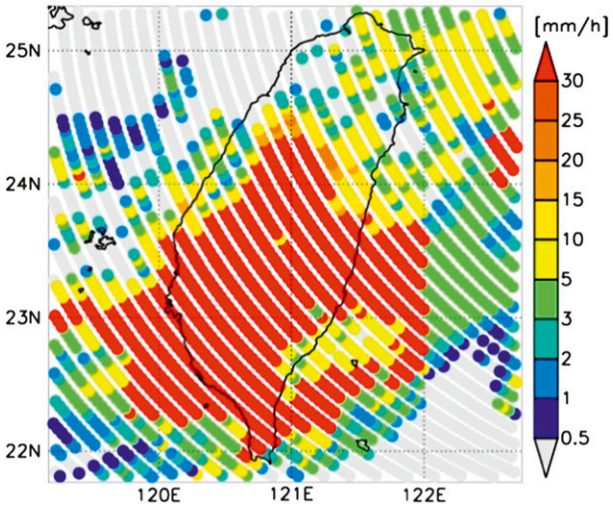

FIG. 3. As in Fig. 1d, but for surface rain rates estimated by the GSMaP_MWR algorithm from the TMI data using LUTs calculated from the orographic rain profiles shown in Figs. 2c and 2d.

layer in the original precipitation profiles is greater than that in the orographic precipitation profiles. Therefore, for a given PCT85, the LUT obtained from the original precipitation profiles gives a rainfall rate that is lower than that obtained from orographic precipitation profiles, leading to an underestimation. Figures 2e and 2f show precipitation profiles over Taiwan obtained from PR data for the case shown in Fig. 1b. Their precipitation top heights are lower than those of the originals (Figs. 2a,b), suggesting that precipitation was enhanced when the moist maritime air was forced by the topography of Taiwan to ascend, causing significant precipitation through the activated warm-rain process, as described above. This is consistent with the results of Tao et al. (2011) who showed that ice processes have only a secondary effect on surface rainfall for Typhoon Morakot based on the sensitivity of physics parameterization schemes in a high-resolution simulation. Therefore, it is reasonable to adopt the orographic precipitation profiles in Figs. 2c and 2d for the Taiwan case.

Figure 3 presents surface rainfall rates estimated by the GSMaP_MWR algorithm from TMI using the LUTs calculated from orographic precipitation profiles. Heavy rainfall not detected by the original GSMaP_MWR algorithm was retrieved, but this shows an overestimation over a broad area. Accordingly, it is necessary to introduce the orographic/nonorographic classification scheme, developed by S13, to determine where to apply the orographic precipitation profiles. The orographic/nonorographic classification scheme is based on the orographically forced upward motion w_{oro} ($m\,s^{-1}$) and moisture flux convergence Q (s^{-1}) as follows:

$$w_{oro} = \frac{Dh}{Dt} = \mathbf{V}_H \cdot \nabla_h \quad \text{and} \tag{1}$$

$$Q = -\nabla \cdot \mathbf{V}_H q, \tag{2}$$

where $\mathbf{V}_H$ is the horizontal surface wind ($m\,s^{-1}$) from JCDAS and q is the water vapor mixing ratio ($kg\,kg^{-1}$) calculated from JCDAS surface specific humidity. Note that in this study, $h(x, y)$ is the elevation (m) derived from the Shuttle Radar Topography Mission (SRTM30; Werner 2001; Farr et al. 2007) with a horizontal grid spacing of approximately 1 km. The orographically forced upward motion determines the location of considerable condensation of water vapor produced in the ascending air mass caused by the orographic effect, while the moisture flux convergence provides sufficient water vapor to sustain the precipitation. S13 defined threshold values for these parameters and then applied the orographic precipitation profiles to those pixels where the threshold conditions were met.

Several studies have suggested that orographic influence on precipitation is described better by a smoothed topography (Pedgley 1970; Vicente et al. 2002; Kwon et al. 2008); thus, it would be better to adopt a smoothed topography in calculating w_{oro}. Therefore, the optimal horizontal length scale for averaging the elevation data as h in Eq. (1) was examined, which was not discussed in S13.

First, we averaged the original elevation data of 1-km horizontal resolution (Fig. 1a) within the horizontal length scale of 10, 50, 80, and 100 km and then calculated w_{oro} using wind data from JCDAS with the minimum time difference from the TRMM observation, as shown in Fig. 4. Note that the wind data were interpolated using the four nearest gridpoint values to calculate w_{oro} at any given point. Next, correlation coefficients between PR 2A25 near-surface rain in Fig. 1b and w_{oro} calculated from Eq. (1) with the elevation averaged within the horizontal length scale of 10, 50, 80, and 100 km, together with the original 1-km resolution data, were examined in the region of upward motion (i.e., positive w_{oro}).

The results are shown in Fig. 5. For original elevation data with 1-km resolution and averaged elevation data within 10 km, the low-resolution wind is equivalent to the constant wind and w_{oro} only represents the detailed topography (Fig. 4a), which results in a weak correlation. On the other hand, for elevation data averaged within 80 and 100 km, w_{oro} does not have maximums (Fig. 4c) that correspond to the marked rainfall rate maximums found in Fig. 1b, resulting in the relatively weak correlation. A relatively high correlation coefficient was obtained for elevation data averaged within 50 km. Compared with Fig. 1b, the areas with upward motion

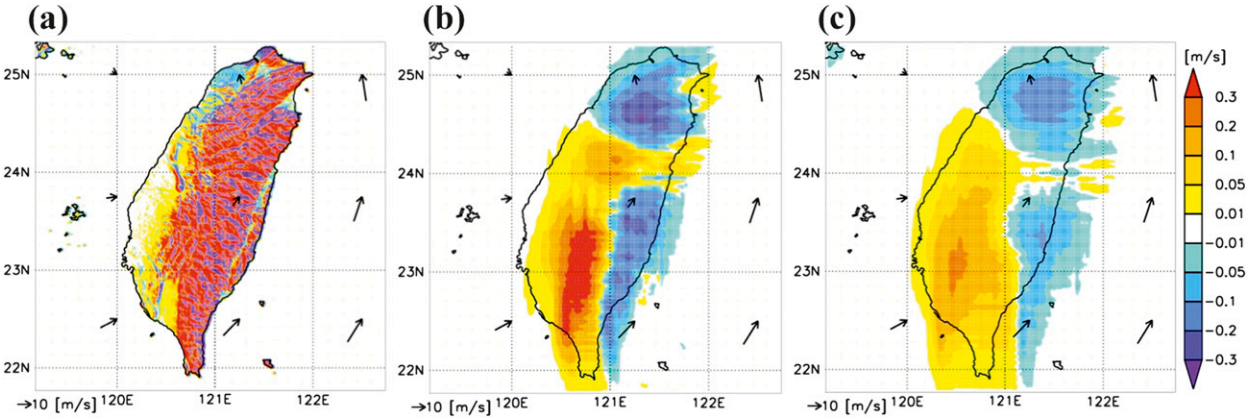

FIG. 4. Orographically forced upward motion w_{oro} ($m\,s^{-1}$) over Taiwan area estimated using Eq. (1) with surface wind data from JCDAS at 1800 UTC 8 Aug 2009 and SRTM30 data: (a) original, 1 km, and averaged within the horizontal length scale of (b) 50 km and (c) 100 km. Vectors are JCDAS surface wind ($m\,s^{-1}$).

stronger than $0.1\,m\,s^{-1}$ in Fig. 4b correspond well to those areas with rainfall rates greater than $20\,mm\,h^{-1}$, and relatively weak rainfall rates are found in those areas with downward motion. Thus, it is inferred that as the air ascends en masse on the horizontal scale, about 50 km in this case, it becomes unstable and convection develops.

Here, we chose to adopt the elevation data averaged within the horizontal length scale of 50 km in calculating w_{oro}. Moisture flux convergence was calculated with the original resolution of the JCDAS data. The entire land of Taiwan is within the convergence region of the moisture flux (i.e., positive Q), and Q was more than $0.5\,s^{-1}$, especially in the heavy rainfall area (not shown), which satisfied the condition of Q for an orographic rainfall pixel in S13. Therefore, we used the same condition for the determination of an orographic rainfall pixel as in S13:

$$w_{oro} > 0.1\ (m\,s^{-1}) \quad \text{and} \quad Q > 0.5 \times 10^{-6}\ (s^{-1}). \qquad (3)$$

For an orographic rainfall pixel determined by condition (3), rainfall rates are estimated using LUTs that are calculated from the orographic precipitation profiles (Figs. 2c,d). On the other hand, for a nonorographic rainfall pixel, rainfall rates are estimated using LUTs that are calculated from the original precipitation profiles (Figs. 2a,b). In this revised GSMaP_MWR algorithm, LUTs calculated from the appropriate precipitation profiles are selected dynamically according to atmospheric conditions derived from 6-hourly JCDAS data, whereas the original algorithm only deals with trimonthly variations in typical hydrometeor profiles.

Figure 6 presents surface rainfall estimated by the GSMaP_MWR algorithm with the orographic/nonorographic rainfall classification scheme. Underestimation on the western slope of the Central Mountain Range in Fig. 1d is greatly improved, and the rainfall distribution pattern in Fig. 1b is also estimated successfully, demonstrating the effectiveness of the GSMaP_MWR algorithm with the orographic/nonorographic rainfall classification scheme.

b. *High-resolution satellite rainfall products*

In this paper, the GSMaP_MWR algorithm with the orographic/nonorographic rainfall classification scheme is applied not only to TMI but also to all spaceborne MWRs: AMSR-E, SSM/I, SSMIS, and AMSU. Note that

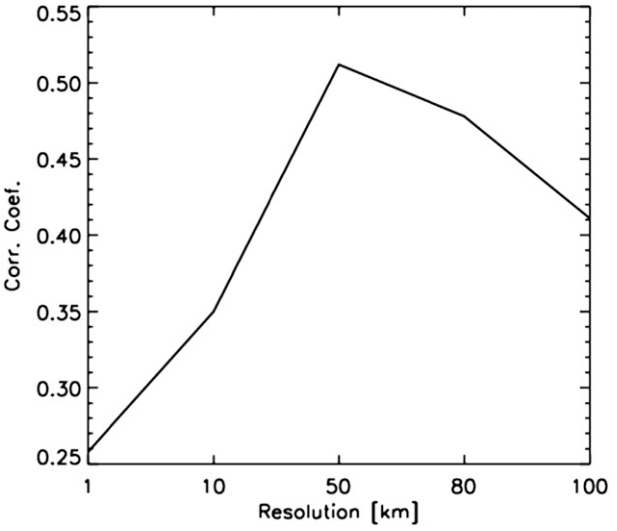

FIG. 5. Correlation coefficients between PR 2A25 near-surface rain shown in Fig. 1b and w_{oro} estimated using elevation data with five horizontal resolutions (1, 10, 50, 80, and 100 km). Calculations for correlation coefficients were made only for the upward motion regions.

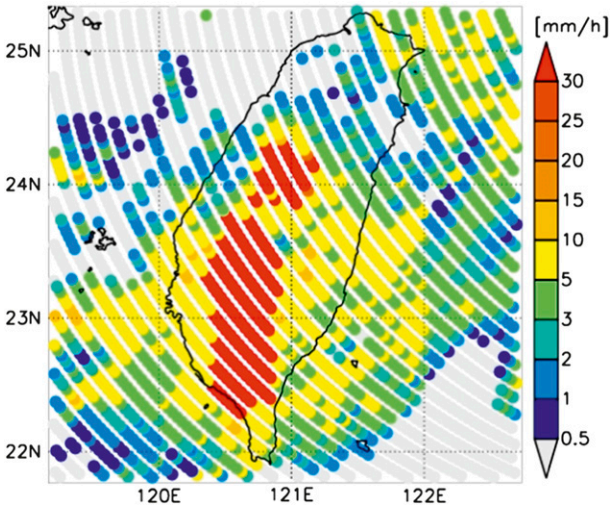

FIG. 6. As in Fig. 1d, but for surface rain rate estimated by the GSMaP_MWR algorithm with the orographic/nonorographic rainfall classification scheme from the TMI data.

the GSMaP_MWR algorithm using sounding channels (Shige et al. 2009) is applied to AMSU, whereas the GSMaP_MWR algorithm using imaging channels (Aonashi et al. 2009) is applied to SSMIS.

High temporal resolution interpolation for the original GSMaP_MWR products and the revised GSMaP_MWR products with the orographic/nonorographic rainfall classification scheme is obtained by cloud-top motion derived from two successive IR images and a Kalman filter (Ushio et al. 2009). Figure 7 shows the time sequence comparison of surface rainfall estimates from the TMPA 3B42RT, the original GSMaP_MVK, and the revised GSMaP_MVK over Taiwan from 1800 UTC 8 August 2009 to 0300 UTC 9 August 2009. Because the temporal resolution of the TMPA 3B42RT product is 3 h, the GSMaP_MVK products with 1-h resolution are averaged over the subsequent 3 h from the data time for comparison. As shown in Fig. 4, the interaction of southwesterly flow with the topography leads to upward motion during this period, which is consistent with previous studies (Ge et al. 2010; Tao et al. 2011), and thereby the revised GSMaP_MWR estimates heavy rainfall using the LUTs calculated from orographic precipitation profiles. Therefore, the revised GSMaP_MVK derived from the revised GSMaP_MWR products estimates continuous heavy rainfall over the mountain area, whereas 3B42RT and the original GSMaP_MVK do not estimate such heavy rain.

Rainfall enhancement in the revised GSMaP_MVK occurs on the eastern side of the mountains (Fig. 7l). Observations derived from a TRMM satellite overpass over Taiwan on 0315 UTC 9 August 2009 (TRMM orbit 66836) indicate that this is an overestimation by the revised GSMaP_MWR due to misclassifying nonorographic rain pixels. One of main reasons for the misclassification is the coarse resolution of JCDAS (1.25° latitude/longitude and 6 hourly).

Rainfall estimates from ground rain gauge observations, the TMPA 3B42RT, the original GSMaP_MVK, and the revised GSMaP_MVK have been accumulated from 0000 UTC 6 August 2009 to 2400 UTC 10 August 2009 to yield a 5-day total rainfall, as shown in Fig. 8, together with the geographical distribution of rain gauge stations over Taiwan. For quantitative comparison, ground rain gauge observations and satellite products were interpolated into a 0.08° latitude and longitude grid.

Both the TMPA 3B42RT and the original GSMaP_MVK products underestimate the enormous amount of rainfall observed by rain gauges for that period. However, the revised GSMaP_MVK estimated successfully such heavy rainfall and its distribution pattern is in good agreement with that of the rain gauge observations, although it is difficult to compare them over the mountain area where there are few rain gauge stations (see Fig. 8f). Conversely, this supports the advantage of satellite observation in detecting heavy rainfall over mountain areas where an observation network is sparse.

Figure 9 shows the comparison of the probability of detection (POD), false alarm ratio (FAR), and the critical success index (CSI). All three products have similar POD, FAR, and CSI values for rainfall thresholds of 100–500 mm. The TMPA 3B42RT has zero values of POD and CSI for rainfall thresholds greater than 800 mm because it does not have rainfall estimates that exceed that threshold (Fig. 8b). The original GSMaP_MVK have rainfall estimates greater than 800 mm (Fig. 8c), but the areas with rainfall estimates greater than 800 mm do not correspond to those observed by rain gauges, resulting in large FAR values, particularly at thresholds of 900 and 1000 mm. The FAR value of the revised GSMaP_MVK increases with threshold, demonstrating that the revised GSMaP_MVK overpredicts the intense rainfall area. However, its FAR values at thresholds of 900 and 1000 mm are lower than those of the original GSMaP_MVK. The revised GSMaP_MVK has much higher CSI values than both the TMPA 3B42RT and the original GSMaP_MVK for rainfall thresholds greater than 1000 mm, demonstrating that the revised GSMaP_MVK has better ability to capture heavy rainfall.

Chen et al. (2013) showed that the CMORPH product (Joyce et al. 2004), as well as the TMPA 3B42RT, poorly estimated the heavy rainfall associated with Typhoon Morakot. The high temporal resolution interpolation of the rainfall estimated using data from MWRs and IR data for the CMORPH product is closer to that for the

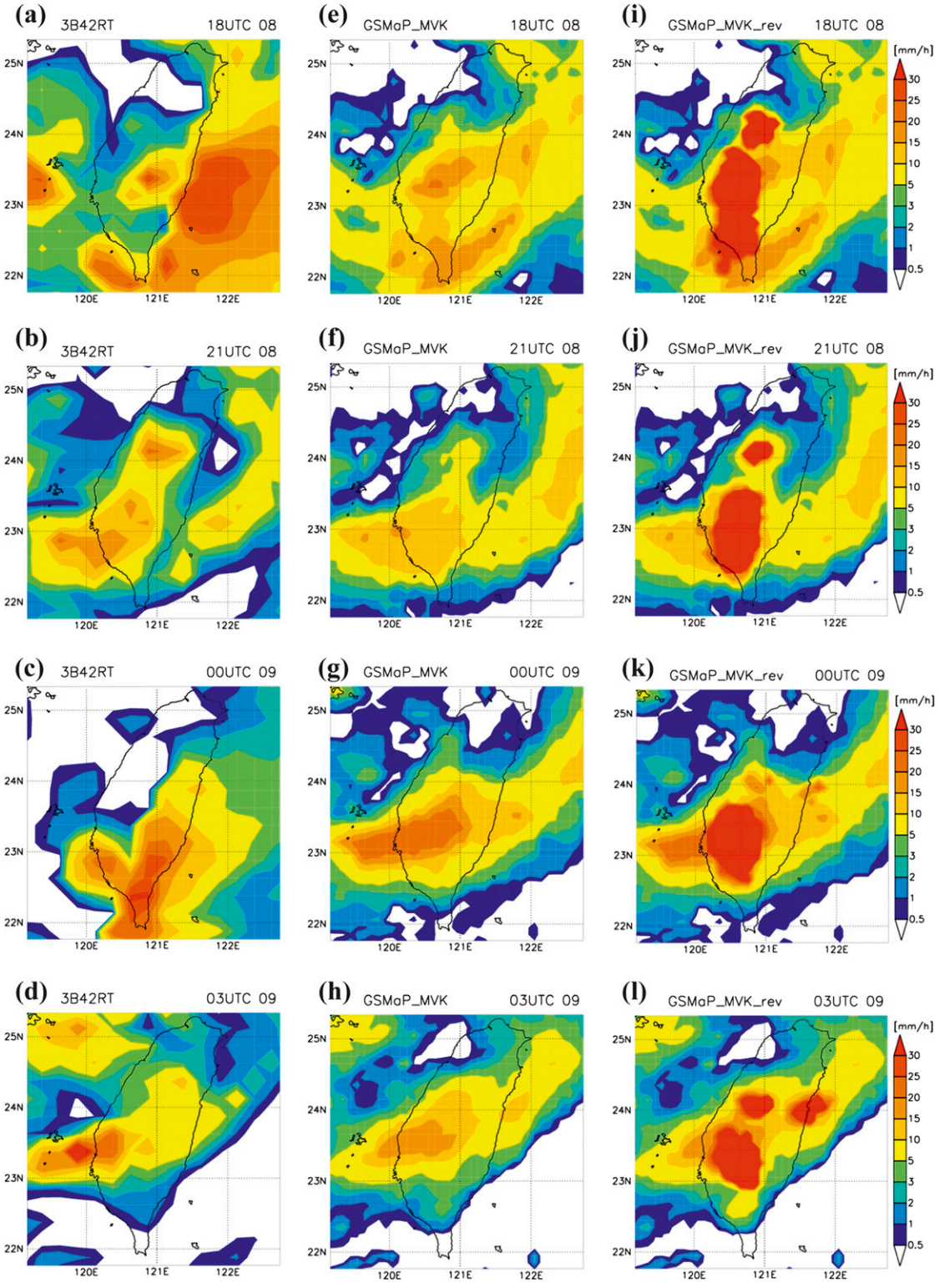

FIG. 7. Consecutive images from 1800 UTC 8 Aug 2009 to 0300 UTC 9 Aug 2009 with 3-hourly intervals from (a)–(d) TMPA 3B42 surface rain (mm h^{-1}), (e)–(h) the original GSMaP_MVK surface rain (mm h^{-1}), and (i)–(l) revised GSMaP_MVK surface rain (mm h^{-1}). The GSMaP_MVK rainfall rates are the averaged values in the next 3 hours from the data time.

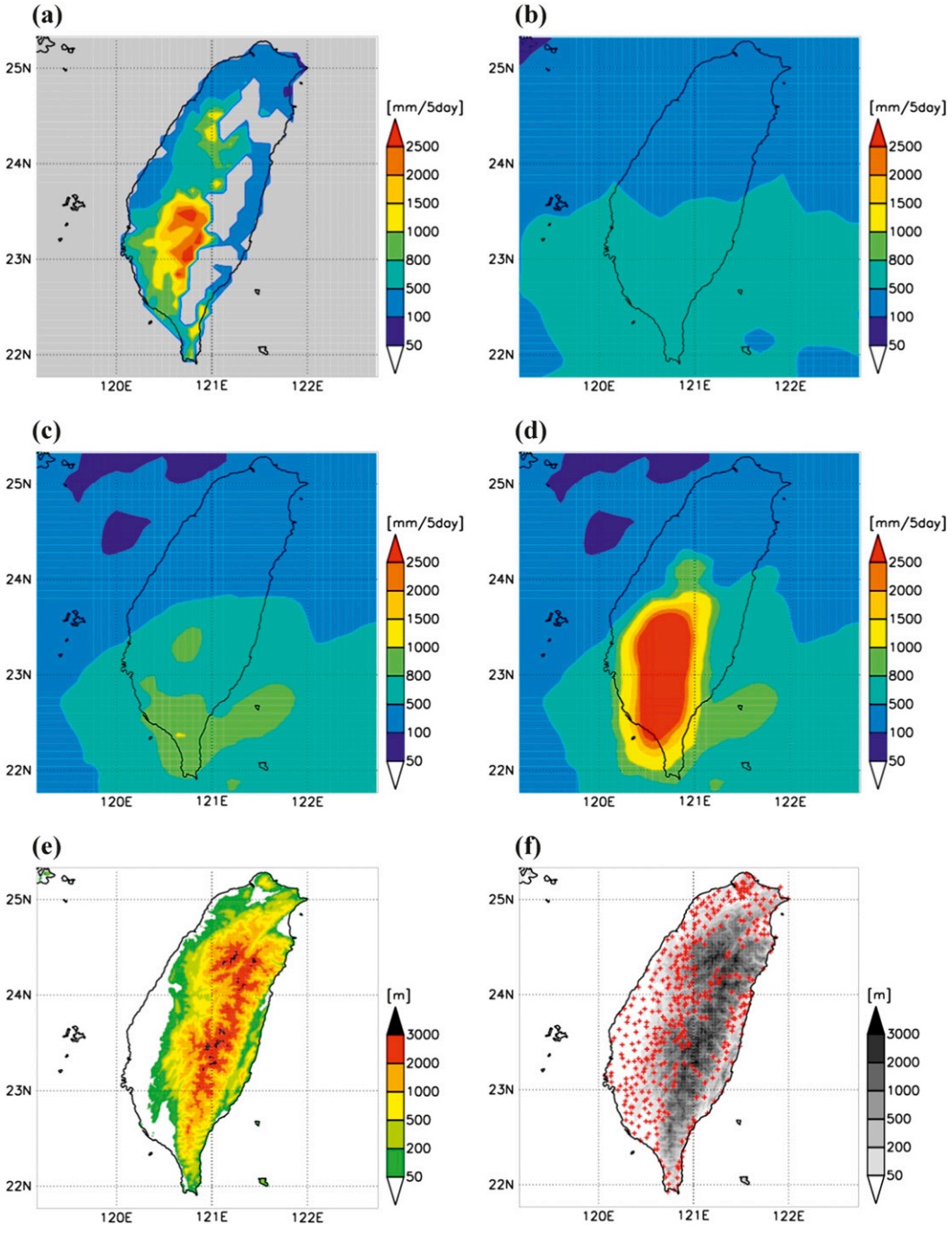

FIG. 8. Accumulated rainfall over Taiwan area from 0000 UTC 6 Aug 2009 to 2400 UTC 10 Aug 2009 [mm (5-days)$^{-1}$] for 0.08° resolution. (a) Rain gauge observations (gray areas in land mean "no data"), (b) TMPA 3B42RT estimates, (c) the original GSMaP_MVK estimates, (d) the revised GSMaP_MVK estimates, (e) SRTM30 elevation (m), and (f) the geographical distribution of rain gauge stations in Taiwan (cross-shape symbols). The shading represents SRTM30 elevation (m).

GSMaP_MVK product than for the TMPA 3B42RT. On the other hand, the CMORPH product shares the rainfall estimated using the GPROF algorithm from MWR data (Fig. 1c) with the TMPA 3B42RT product. Therefore, the main reason for failing to estimate heavy rainfall associated with Typhoon Morakot is due to the MRW algorithm, rather than the technique of combining MWR and IR data, which is consistent with the findings

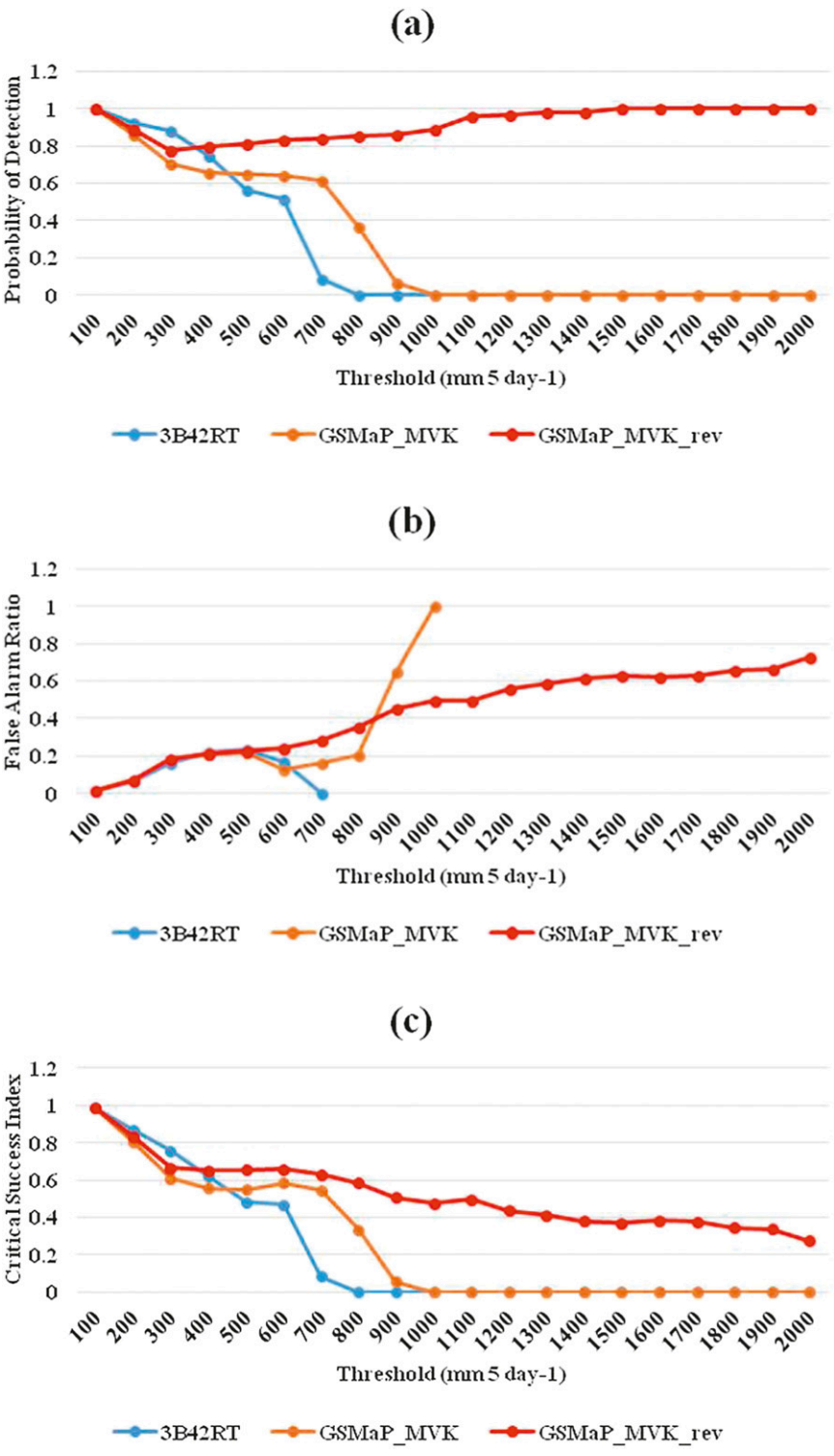

FIG. 9. Comparison of (a) POD, (b) FAR, and (c) CSI based on different rainfall thresholds [mm $(5\text{-days})^{-1}$].

of Kubota et al. (2009). Note that the results of the GSMaP_MVK near-real-time version product, where the Kalman filter model is applied only to the propagation process forwards in time, are almost the same as those of the GSMaP_MVK product, where the Kalman filter model is applied to the propagation process forwards and backward in time. On the other hand, Chen et al. (2013) showed that the TMPA 3B42, which is adjusted by gauged measurements, presented less heavy rainfall than the TMPA 3B42RT, probably because of the process of rescaling the TMPA 3B42RT to the monthly rain gauge data.

As signals of heavy rainfall are indispensable for flood and landslide analysis/prediction applications (Harris et al. 2007; Hong et al. 2007), it is a remarkable advance for these applications that the revised GSMaP algorithm succeeds in detecting heavy orographic rainfall continuously in the sense of time and space, while the present algorithms fail. The results indicate that the revised GSMaP algorithm is quite effective for the Taiwan case if the horizontal length scale for averaging the elevation data is appropriate for calculating w_{oro} and if the thresholds in Eq. (3) are chosen properly. These would be a primary issue for future study. The horizontal length scale and thresholds appropriate for the orographic/nonorographic rainfall classification scheme might vary with differing situations (topography, wind speeds, etc.), and they must be determined objectively. Moreover, another issue that is not addressed is the precipitation profiles used in the forward calculating part of the GSMaP_MWR algorithm. The orographic precipitation profiles (Figs. 2c,d) used in the revised GSMaP_MWR have extremely low precipitation top heights compared with the actual precipitation profiles in this Taiwan case, as derived from PR data (Figs. 2e,f), and this might lead to an overestimation. Thus, there is the need to construct more representative orographic precipitation profiles for better estimations by analyzing the relationships between those parameters that represent orographic effects, such as the orographically forced upward motion, and those properties of vertical hydrometeor structures obtained from PR observation such as the precipitation water path (Masunaga et al. 2002).

4. Summary

The GSMaP_MWR algorithm with the orographic/nonorographic rainfall classification scheme, developed by S13, is applied for Typhoon Morakot (2009), for which the current satellite rainfall products have been shown in a previous study to estimate poorly the heavy rainfall (Chen et al. 2013). The classification scheme is based on orographically forced upward motion and moisture flux convergence, which are calculated from elevation and JCDAS data.

According to the correlation between the PR surface rain and orographically forced upward motion calculated from terrain data averaged within various horizontal length scales, there is an optimal horizontal length scale at which the air ascends en masse, becomes unstable, and then convection develops. The GSMaP_MWR algorithm with the orographic/nonorographic rainfall classification scheme estimates successfully the heavy orographic rainfall associated with Typhoon Morakot, and the underestimation by the present GSMaP_MWR algorithm was improved significantly. Applying the revised GSMaP_MWR algorithm to all MWRs (imagers and sounders) and combining them with IR data using the GSMaP_MVK algorithm, we succeed in estimating the heavy orographic rainfall associated with Typhoon Morakot with high temporal and spatial resolution.

The results suggest that this revised algorithm is effective for the improvement of rainfall estimates over mountainous areas when the resolution of the elevation data and the thresholds to decide the original precipitation profiles, or the orographic precipitation profiles, are chosen properly. However, the orographic rain profiles used for the improvement have quite low precipitation top heights, which might lead to overestimation in some cases. For better estimates, it is necessary to construct more representative profiles of orographic rainfall, to investigate the optimum horizontal length scale for averaging the elevation data used in calculating the orographically forced upward motion, and to determine a proper threshold to decide where to apply the orographic precipitation profiles. For the GSMaP products, which are available in near real time (about 4 hours after observation) via the Internet (Kachi et al. 2011), analysis data such as the JMA global analysis or forecasting data should be used instead of the reanalysis data used here. Despite these remaining issues, this study shows a remarkable advance in high-resolution satellite rainfall products and in the possibility of their application to flood and landslide analysis/prediction because signals of heavy rainfall are vital for these applications (Harris et al. 2007; Hong et al. 2007). The revised GSMaP algorithm succeeds in detecting heavy orographic rainfall continuously in the sense of time and space.

Acknowledgments. This study is supported by the Earth Observation Research Center, the Japan Aerospace Exploration Agency, a Grant-in-Aid for Scientific Research (KAKENHI), and the Environment Fund of Mitsui and Co., Ltd. The authors thank the three anonymous reviewers for their constructive comments that helped improve the clarity of the paper.

APPENDIX

Definitions of Acronyms

AMSR-E	Advanced Microwave Scanning Radiometer for the Earth Observing System
AMSU	Advanced Microwave Sounding Unit
CMORPH	Climate Prediction Center Morphing
CSI	Critical success index
FAR	False alarm ratio
FLH	Freezing-level height
GPROF	Goddard profiling
GSMaP	Global Satellite Mapping of Precipitation
GSMaP_MVK	GSMaP algorithm based on moving vector with Kalman filter
GSMaP_MWR	GSMaP algorithm for microwave radiometers
IR	Infrared radiometer
JCDAS	JMA Climate Data Assimilation System
JMA	Japan Meteorological Agency
JRA-25	Japanese 25-yr Reanalysis
LUT	Lookup table
MWR	Microwave radiometer
PCT85	Polarization-corrected temperatures at 85 GHz
POD	Probability of detection
PR	Precipitation Radar
RTM	Radiative transfer model
SRTM30	Shuttle Radar Topography Mission 30 arc-second elevation
SSM/I	Special Sensor Microwave Imager
SSMIS	Special Sensor Microwave Imager/Sounder
TMI	TRMM Microwave Imager
TMPA	TRMM Multisatellite Precipitation Analysis
TMPA 3B42RT	TMPA 3B42 near-real-time version product
TRMM	Tropical Rainfall Measuring Mission

REFERENCES

Aonashi, K., and Coauthors, 2009: GSMaP passive microwave precipitation retrieval algorithm: Algorithm description and validation. *J. Meteor. Soc. Japan,* **87A,** 119–136, doi:10.2151/jmsj.87A.119.

Chen, S., and Coauthors, 2013: Performance evaluation of radar and satellite rainfalls for Typhoon Morakot over Taiwan: Are remote-sensing products ready for gauge denial scenario of extreme events? *J. Hydrol.,* doi:10.1016/j.jhydrol.2012.12.026, in press.

Dinku, T., S. J. Connor, and P. Ceccato, 2010: Comparison of CMORPH and TRMM-3B42 over mountainous regions of Africa and South America. *Satellite Rainfall Applications for Surface Hydrology,* Springer, 193–204.

Farr, T. G., and Coauthors, 2007: The shuttle radar topography mission. *Rev. Geophys.,* **45,** RG2004, doi:10.1029/2005RG000183.

Ge, X., T. Li, S. Zhang, and M. Peng, 2010: What causes the extremely heavy rainfall in Taiwan during Typhoon Morakot (2009)? *Atmos. Sci. Lett.,* **11,** 46–50.

Gebremichael, M., and F. Hossain, Eds., 2010: *Satellite Rainfall Applications for Surface Hydrology.* Springer, 327 pp.

Harris, A., S. Rahman, F. Hossain, L. Yarborough, A. C. Bagtzoglou, and G. Easson, 2007: Satellite-based flood modeling using TRMM-based rainfall products. *Sensors,* **7,** 3416–3427, doi:10.3390/s7123416.

Hong, Y., R. F. Alder, A. Negri, and G. J. Huffman, 2007: Flood and landslide applications of near real-time satellite rainfall products. *Nat. Hazards,* **43,** 285–294, doi:10.1007/s11069-006-9106-x.

Huffman, G. J., R. F. Adler, D. T. Bolvin, G. Gu, E. J. Nelkin, K. P. Bowman, E. F. Stocker, and D. B. Wolff, 2007: The TRMM Multisatellite Precipitation Analysis (TMPA): Quasi-global, multi-year, combined-sensor precipitation estimates at fine scales. *J. Hydrometeor.,* **8,** 38–55, doi:10.1175/JHM560.1.

Iguchi, T., T. Kozu, J. Kwiatkowski, R. Meneghini, J. Awaka, and K. Okamoto, 2009: Uncertainties in the rain profiling algorithm for the TRMM precipitation radar. *J. Meteor. Soc. Japan,* **87A,** 1–30, doi:10.2151/jmsj.87A.1.

Joyce, R. J., J. E. Janowiak, P. A. Arkin, and P. Xie, 2004: CMORPH: A method that produces global precipitation estimates from passive microwave and infrared data at high spatial and temporal resolution. *J. Hydrometeor.,* **5,** 487–503, doi:10.1175/1525-7541(2004)005<0487:CAMTPG>2.0.CO;2.

Kachi, M., T. Kubota, T. Ushio, S. Shige, S. Kida, K. Aonashi, K. Okamoto, and R. Oki, 2011: Development and utilization of ''JAXA global rainfall watch'' system based on combined microwave and infrared radiometers aboard satellites (in Japanese). *IEEJ Trans. Fundam. Mater.,* **131,** 729–737, doi:10.1541/ieejfms.131.729.

Kozu, T., and Coauthors, 2001: Development of precipitation radar onboard the Tropical Rainfall Measuring Mission (TRMM) satellite. *IEEE Trans. Geosci. Remote Sens.,* **39,** 102–116, doi:10.1109/36.898669.

Kubota, T., and Coauthors, 2007: Global precipitation map using satellite-borne microwave radiometers by the GSMaP project: Production and validation. *IEEE Trans. Geosci. Remote Sens.,* **45,** 2259–2275, doi:10.1109/TGRS.2007.895337.

——, T. Ushio, S. Shige, S. Kida, M. Kachi, and K. Okamoto, 2009: Verification of high-resolution satellite-based rainfall estimates around Japan using a gauge-calibrated ground-radar dataset. *J. Meteor. Soc. Japan,* **87A,** 203–222, doi:10.2151/jmsj.87A.203.

Kummerow, C., W. Barnes, T. Kozu, J. Shiue, and J. Simpson, 1998: The Tropical Rainfall Measuring Mission (TRMM) sensor package. *J. Atmos. Oceanic Technol.,* **15,** 809–816, doi:10.1175/1520-0426(1998)015<0809:TTRMMT>2.0.CO;2.

——, and Coauthors, 2001: The evolution of the Goddard profiling algorithm (GPROF) for rainfall estimation from passive microwave sensors. *J. Appl. Meteor.,* **40,** 1801–1820, doi:10.1175/1520-0450(2001)040<1801:TEOTGP>2.0.CO;2.

Kwon, E.-H., B.-J. Sohn, D.-E. Chang, M.-H. Ahn, and S. Yang, 2008: Use of numerical forecasts for improving TMI rain retrievals over the mountainous area in Korea. *J. Appl. Meteor. Climatol.,* **47,** 1995–2007, doi:10.1175/2007JAMC1857.1.

Liu, G., 1998: A fast and accurate model for microwave radiance calculations. *J. Meteor. Soc. Japan,* **76,** 335–343.

Masunaga, H., T. Iguchi, R. Oki, and M. Kachi, 2002: Comparison of rainfall products derived from TRMM Microwave Imager and precipitation radar. *J. Appl. Meteor.,* **41,** 849–862, doi:10.1175/1520-0450(2002)041<0849:CORPDF>2.0.CO;2.

McCollum, J. R., and R. R. Ferraro, 2003: Next generation of NOAA/NESDIS TMI, SSM/I, and AMSR-E microwave land rainfall algorithms. *J. Geophys. Res.,* **108,** 8382, doi:10.1029/2001JD001512.

Negri, A. J., and R. F. Adler, 1993: An intercomparison of three satellite infrared rainfall techniques over Japan and surrounding waters. *J. Appl. Meteor.,* **32,** 357–373, doi:10.1175/1520-0450(1993)032<0357:AIOTSI>2.0.CO;2.

Okamoto, K., 2003: A short history of the TRMM precipitation radar. *Cloud Systems, Hurricanes and the Tropical Rainfall Measurement Mission (TRMM): A Tribute to Dr. Joanne Simpson, Meteor. Monogr.,* No. 51, Amer. Meteor. Soc., 187–195, doi:10.1175/0065-9401(2003)029<0187:CASHOT>2.0.CO;2.

Olson, W. S., and Coauthors, 2006: Precipitation and latent heating distributions from satellite passive microwave radiometry. Part I: Method and uncertainty estimates. *J. Appl. Meteor. Climatol.,* **45,** 702–720, doi:10.1175/JAM2369.1.

Onogi, K., and Coauthors, 2007: The JRA-25 Reanalysis. *J. Meteor. Soc. Japan,* **85,** 369–432, doi:10.2151/jmsj.85.369.

Pedgley, D. E., 1970: Heavy rainfalls over Snowdonia. *Weather,* **25,** 340–350, doi:10.1002/j.1477-8696.1970.tb04117.x.

Sakakibara, H., 1981: Heavy rainfall from very shallow convective clouds. *J. Meteor. Soc. Japan,* **59,** 387–394.

Shige, S., and Coauthors, 2009: The GSMaP precipitation retrieval algorithm for microwave sounders. Part I: Over-ocean algorithm. *IEEE Trans. Geosci. Remote Sens.,* **47,** 3084–3097, doi:10.1109/TGRS.2009.2019954.

——, S. Kida, H. Ashiwake, T. Kubota, and K. Aonashi, 2013: Improvement of TMI rain retrievals in mountainous areas. *J. Appl. Meteor. Climatol.,* **52,** 242–254, doi:10.1175/JAMC-D-12-074.1.

Sorooshian, S., K.-L. Hsu, X. Gao, H. V. Gupta, B. Imam, and D. Braithwaite, 2000: Evaluation of PERSIANN system satellite-based estimates of tropical rainfall. *Bull. Amer. Meteor. Soc.,* **81,** 2035–2046, doi:10.1175/1520-0477(2000)081<2035:EOPSSE>2.3.CO;2.

Spencer, R. W., H. M. Goodman, and R. E. Hood, 1989: Precipitation retrieval over land and ocean with SSM/I: Identification and characteristics of the scattering signal. *J. Atmos. Oceanic Technol.,* **6,** 254–273, doi:10.1175/1520-0426(1989)006<0254:PROLAO>2.0.CO;2.

Takayabu, Y. N., 2006: Rain-yield per flash calculated from TRMM PR and LIS data and its relationship to the contribution of tall convective rain. *Geophys. Res. Lett.,* **33,** L18705, doi:10.1029/2006GL027531.

——, 2008: Observing rainfall regimes using TRMM PR and LIS data. GEWEX News, No. 18, International GEWEX Project Office, Silver Spring, MD, 9–10.

Takeda, T., and K. Takase, 1980: Radar observation of rainfall system modified by orographic effects. *J. Meteor. Soc. Japan,* **58,** 500–516.

——, N. Moriyama, and Y. Iwasaka, 1976: A case study of heavy rain in Owase area. *J. Meteor. Soc. Japan,* **54,** 32–41.

Tao, W.-K., and Coauthors, 2011: High resolution numerical simulation of the extreme rainfall associated with Typhoon Morakot. Part I: Comparing the impact of microphysics and PBL parameterizations with observations. *Terr. Atmos. Ocean. Sci.,* **22,** 673–696, doi:10.3319/TAO.2011.08.26.01(TM).

Ushio, T., and Coauthors, 2009: A Kalman filter approach to the Global Satellite Mapping of Precipitation (GSMaP) from combined passive microwave and infrared radiometric data. *J. Meteor. Soc. Japan,* **87A,** 137–151, doi:10.2151/jmsj.87A.137.

Vicente, G. A., J. C. Davenport, and R. A. Scofield, 2002: The role of orographic and parallax corrections on real-time high-resolution satellite rainfall rate distribution. *Int. J. Remote Sens.,* **23,** 221–230, doi:10.1080/01431160010006935.

Wang, N. Y., C. Liu, R. Ferraro, D. Wolff, E. Zipser, and C. Kummerow, 2009: TRMM 2A12 land precipitation product-status and future plans. *J. Meteor. Soc. Japan,* **87A,** 237–253, doi:10.2151/jmsj.87A.237.

Werner, M., 2001: Shuttle Radar Topography Mission (SRTM) mission overview. *J. Telecommun. (Frequenz),* **55,** 75–79.

Wu, C.-C., 2013: Typhoon Morakot: Key findings from the journal *TAO* for improving prediction of extreme rains at landfall. *Bull. Amer. Meteor. Soc.,* **94,** 155–160, doi:10.1175/BAMS-D-11-00155.1.

——, and M. J. Yang, 2011: Preface to the special issue on ''Typhoon Morakot (2009): Observation, modeling, and forecasting.'' *Terr. Atmos. Ocean. Sci.,* **22,** doi:10.3319/TAO.2011.10.01.01(TM).